HOSTED BY

ELSEVIER

CrossMark

Available online at www.sciencedirect.com

ScienceDirect

Progress in Natural Science: Materials International 24 (2014) 492–499

Progress in Natural Science Materials International

www.elsevier.com/locate/pnsmi
www.sciencedirect.com

Original Research

In vitro corrosion of Mg–1.21Li–1.12Ca–1Y alloy

Rongchang Zeng[a,b,*], Weichen Qi[a], Fen Zhang[a], Hongzhi Cui[a], Yufeng Zheng[c]

[a]College of Materials Science and Engineering, Shandong University of Science and Technology, Qingdao 266590, China
[b]State Key Laboratory of Mining Disaster Prevention and Control Co-founded by Shandong Province and the Ministry of Science and Technology, Shandong University of Science and Technology, Qingdao 266590, China
[c]State Key Laboratory for Turbulence and Complex System, Department of Materials Science and Engineering, College of Engineering, Peking University, Beijing 100871, China

Received 2 July 2014; accepted 1 September 2014
Available online 18 October 2014

Abstract

The influence of the microstructure on mechanical properties and corrosion behavior of the Mg–1.21Li–1.12Ca–1Y alloy was investigated using OM, SEM, XRD, EPMA, EDS, tensile tests and corrosion measurements. The results demonstrated that the microstructure of the Mg–1.21Li–1.12Ca–1Y alloy was characterized by α-Mg substrate and intermetallic compounds Mg_2Ca and $Mg_{24}Y_5$. Most of the fine Mg_2Ca particles for the as-cast alloy were distributed along the grain boundaries, while for the as-extruded along the extrusion direction. The $Mg_{24}Y_5$ particles with a larger size than the Mg_2Ca particles were positioned inside the grains. The mechanical properties of Mg–1.21Li–1.12Ca–1Y alloy were improved by the grain refinement and dispersion strengthening. Corrosion pits initiated at the α-Mg matrix neighboring the Mg_2Ca particles and subsequently the alloy exhibited general corrosion and filiform corrosion as the corrosion product layer of $Mg(OH)_2$ and $MgCO_3$ became compact and thick.

Keywords: Magnesium–lithium alloys; Microstructure; Mechanical property; Corrosion; Biomaterial

1. Introduction

Magnesium alloys can degrade naturally in vivo and their unique mechanical properties also render them desirable biodegradable implants [1,2]. However, based on the prior clinical studies [3], the major shortcoming is that the magnesium alloys degrade too rapid to be the biodegradable implants. Thus, it is of importance to tailor the corrosion rate of magnesium alloys to ensure the request of the clinic implantation.

Generally, surface modification and element alloying are the two approaches to improvement in the corrosion resistance of magnesium alloys. Surface modifications [4,5] such as Ca–P or HA coating [6–8], chemical conversion coating [8–10] and polymeric coating [11–13] and micro-arc oxidation [14,15] have been developed. Nevertheless, there are numerous issues involving the adhesion bonding between the Ca–P coatings and their substrates, biocompatibility of the chemical conversion coatings, swelling for the polymeric coating. Therefore, surface modification cannot completely face the challenge for the reduction in corrosion rate [8,9,11,12].

Element alloying, however, still plays the most important role on the manipulation of the corrosion resistance of biomedical magnesium alloys [1,16]. Taking mechanical compatibility and biocompatibility into consideration the commercial magnesium alloys do not satisfy the requirements for mechanical properties and corrosion resistance of the degradable implants as well as biocompatibility. For example, cardiovascular stents necessitate enhanced ductility and corrosion resistance. Thus, a considerable kind of novel magnesium alloys such as Mg–Ca [17,18], Mg–Zn–Ca [19,20], Mg–Mn–Zn [21], Mg–Nd–Zn–Zr [22,23] and Mg–Zn–Mn–Ca [24] have been investigated for the purpose of biomedical applications.

Interestingly, Mg–Li alloy (i.e., LAE442) possesses a superior in vivo corrosion resistance in comparison to AZ31, AZ91D and

*Corresponding author. Tel.: +86 532 80681226; fax: +86 532 86057920.
E-mail address: rczeng@foxmail.com (R. Zeng).
Peer review under responsibility of Chinese Materials Research Society.

http://dx.doi.org/10.1016/j.pnsc.2014.08.005
1002-0071/

WE43 [25]. So far, the probes have been focused on the in vitro and in vivo corrosion and corrosion protection, biocompatibility of Mg–Li–(Al)–(RE) alloys including LAE442 alloy [26–29]. The results demonstrate that these Mg–Li based alloys were promising potential biodegradable biomaterials. However, these alloys contain a higher content of Al, which is toxic to body tissue [4]. Thus, aluminum-free magnesium–lithium based alloys are screened as potential implantation materials. Our previous studies indicate that Mg–Li–Ca alloys maybe one of the candidate materials [30,31].

It is well-known that the introduction of elemental Li can change the structure of magnesium [32]. The unique property is attributed to a decrease in the lattice constant ratio (c/a) with an increasing Li content, which activates non-basal slip planes and results in a significant increase in the volume fraction of the body-centered cubic (bcc) structure [31,33].

Moreover, Ca is one of the major component element in human body, it can refine the microstructure and improve the strength by forming the intermetallic compound Mg_2Ca [30]. Unfortunately, issues on the role of Ca played in magnesium corrosion are still highly controversial. Song [34] suggested that Ca has no significant influence on the corrosion of magnesium. While, Kim [35] reported that Ca accelerates the corrosion of magnesium due to the presence of micro-galvanic corrosion between the Mg_2Ca phase and the α-Mg phase. Li [36] claimed that an increasing Ca content improves the compressive strength, elastic modulus and hardness of the Mg–Ca alloys, but deteriorates the ductility, corrosion resistance and biocompatibility of the Mg–Ca alloys. It is generally recognized that Mg–Ca alloys with Ca additions less than 1.0 wt% exhibit a good biocompatibility, low corrosion rate as well as appropriate elastic modulus and strength [37].

Furthermore, RE-containing magnesium alloys such as WE43 [38,39], Mg–Y [40,41], Mg–14Li–1Al–0.3Y [27], Mg–14Li–*x*Sr [42] and LAE442 [25] have been investigated. RE elements tend to form a variety of intermetallic compounds. For instance, $Al_{11}RE_3$ is the main precipitated phase in the LAE442 alloy [38], while $Mg_{24}Y_5$ and Mg_2Y are formed in the Mg–Y alloys [43,44]. The $Mg_{24}Y_5$ phase has a precipitation hardening effect in the Mg–Y alloy [44]. Y can improve the mechanical properties and retard the biodegradation of Mg alloys [45,46]. However, it also found that the Y addition leads to an increase in the ductility, but a decrease in the compressive strength, hardness, corrosion resistance and biocompatibility of the Mg–1Ca–1Y alloy when compared to the Mg–1Ca alloy [36]. These results disclose the issues of the roles of the oxide film and the intermetallic compounds on the influence of Y on corrosion behavior of the alloys.

On one hand, Y-containing surface oxide layer improves the corrosion resistance due to the fact that Y is prone to segregate in the outer surface of Mg alloys [31,47,48], and form a compact oxide film with a spinel structure of Y_2O_3 ● MgO. On the other hand, the Y-containing secondary phase, i.e., $Mg_{24}Y_5$, accelerates the micro-galvanic corrosion simultaneously. The corrosion resistance of binary Mg–Y alloys is reduced with the increment of precipitate phase $Mg_{24}Y_5$ [40,41]. Thus, the influence of the Y concentration on corrosion resistance is paradoxical [49,50], depending on the compositions of Mg alloys and the concentration of Y together with the species of the solution. In 0.1 M NaCl, the corrosion rate increases with increasing Y content due to an increase in the amount of the Y-containing intermetallic compounds. In 0.1 M Na_2SO_4, the corrosion rate decreases with increasing Y content over 3 wt%, attributed to a more protective surface film, despite the intermetallic compounds [47].

It should be noted that a very small amount of low toxicity rare earth can be tolerated in the human body [14]. For instance, HA doped with a concentration of 2.5 mol% Y^{3+} shows an excellent biocompatibility [49]. Mg–0.5Ca, Mg–1Ca and Mg–1Ca–1Y alloys are bio-compatible alloys. The Mg–1Ca–1Y alloy shows the same level of cell viability and proliferation, compared to the Mg–1Ca alloy [36].

So far, the research on ternary Mg–Li–Ca alloy has been concentrated. Our previous study [30] indicates that Mg–Li–Ca alloys have lower pH values and better corrosion resistance in Hank's solutions compared with Mg–Ca alloys and our subsequent study [31] also demonstrates that both α-Mg and β-Li phases of the Mg–Li–Ca alloys are simultaneously subjected to corrosion, whereas for the other alloys such as Mg–Al alloys, only the α-Mg matrix is attacked. Ardelean [39] suggested that the elements, including Nd, Zr and Y, play a positive role on improving corrosion resistance of the WE 43 alloy compared with pure Mg.

Therefore, it is postulated that the addition of Y into the Mg–Li–Ca alloy could improve the mechanical properties and corrosion properties of magnesium alloy in comparison to Mg–Li–Ca alloy for biomedical purpose on the basis of the unique characteristics of Y element. Unfortunately, no literatures regarding the corrosion of the Mg–Li–Ca–Y alloy is available [3,14]. The purpose of the paper is to compare the influence of processing on the microstructure and mechanical property of the as-extruded Mg–Li–Ca–Y alloy and the as-cast alloy, and to gain further insight into the corrosion mechanism of the alloy.

2. Experimental

2.1. Materials

The cast Mg–1.21wt%Li–1.12wt%Ca–Y ingots were fabricated in the Institute of Metals Research, Chinese Academy of Sciences. The ingots were extruded into the sheets on an extrusion machine (Yuanhang, 800 t) at the Magnesium Industry in Chongqing Science and Technology Company, Ltd., with an extrusion ratio of 20.4:1 and an extrusion rate of 1 m/min. The mold and the ingots were heated up to the temperature of 350 °C and 300 °C, respectively.

2.2. Corrosion characterization

The dimension of the corrosion test samples was 45 mm × 26 mm × 4 mm. Before the immersion test, the samples were ground to 1200 grit, degreased in acetone, and dried in warm air. All immersion tests were repeated three times to obtain reproducible results in 37 °C and the medium-to-sample-area ratio is 20 ml/cm^2. At the end of the experiment, final cleaning of the sample was carried out by dipping it into the solution

(200 g Cr_2O_3, 10 g $AgNO_3$, 20 g $Ba(NO_3)_2$ and 1000 ml distilled water) for 5 min followed by washing with water. Then corrosion rate was calculated according to the weight loss. The hydrogen evolution rate (HER) was evaluated by the gas collection, which detailed information was reported in the literature [31]. The pH values of the solutions were recorded at an interval of 10 min in the first 4 h, and at an interval of 20 min thereafter by a pH meter (PHS-25 type).

The electrochemical corrosion behavior of the samples was studied using a electrochemical workstation (EG&G model 273). Prior to the experiment, the samples were ground up to 1200 grit, and then washed with distilled water and acetone. Polarization measurements were carried out in a corrosion cell containing 400 ml of Hank's solution (Table 1) using a standard three-electrode system. A saturated calomel electrode (SCE) was used as a reference with a platinum counter electrode. The exposed area of working electrode was 2.84 cm^2. Potentiodynamic polarization curves were measured after an immersion of 5 min. The scanning potentials ranged between $\pm$300 mV at a scan rate of 1 mV/s. The triplicated tests were conducted for each alloy.

2.3. Tensile test

The tensile tests were performed on a CMT5105 type tensile machine at a strain rate of 3 mm/min at room temperature according to the standard GB/T228-2002. The gauge length and width were 25 mm and 6 mm, respectively.

2.4. Surface analysis

Scanning electron microscopy (SEM, KYKY-2800B) was employed to discern the surface morphology of the Mg–1.21Li–1.12Ca–1Y alloy. The elemental distribution of the alloy was probed using electron microprobe analysis (EMPA, JXA-8230). The phase composition was examined by means of X-ray diffraction (XRD, D/Max2500PC).

3. Results

3.1. Change in microstructure

The microstructure (Fig. 1a) of the as-cast Mg–1.21Li–1.12Ca–1Y alloy is characterized by the coarse grained α-Mg with intermetallic compounds Mg_2Ca and $Mg_{24}Y_5$, distributed along the grain boundaries (GBs) and within the grains (Fig. 1a and b). While the refined and elongated grains are developed in the extruded Mg–1.21Li–1.12Ca–1Y alloy (Fig. 1c and d). Particularly, the Mg_2Ca particles distribute along the extrusion direction (Fig. 1d).

In addition, the intermetallic compounds $Mg_{24}Y_5$ (Fig. 2a) and Mg_2Ca (Fig. 2b) are identified by EDS. Obviously, the amount of the Mg_2Ca particles is higher than that of the $Mg_{24}Y_5$ particles. The size of the Mg_2Ca particles is relatively smaller than that of the $Mg_{24}Y_5$ particles.

The insets in Fig. 2 designate the EDS results of the intermetallic compounds in the as-cast alloy. The EDS results indicate that white particles in the grain interior are the $Mg_{24}Y_5$ phase (Fig. 2a). The size of Mg_2Ca particle in the as-cast alloy is larger than as-extruded one, which has been showed in Fig. 2b. It is found that there is also a trace of Y element that exists in the Mg_2Ca particles.

Similarly, the intermetallic compounds in the as-extruded alloy were identified by EPMA and EDS (Fig. 3) and the EDS results are listed in Table 2. The EDS results show grain interior and the grain boundaries (GBs) (Spectra 1 and 2) with a pretty low level of Ca and without Ca, respectively. The compound Mg_2Ca is mainly distributed at GBs, which fell off and left a series of scattered pits. The white granular and reticular particles (Spectrum 3) on the image may be the $Mg_{24}Y_5$ phase or MgO or Y_2O_3 oxides or their mixture [44] based on the element ratio of Mg, Y and O. The low electrical conductivity of intermetallic compounds appears in white color in the SEM image. The pearl-chain-like scattered Mg_2Ca particles (Spectrum 4) are generally observed in the extruded Mg alloys (Fig. 3a and b).

3.2. Changes in mechanical properties

Due to greater total GB areas, the refined microstructure enhances the mechanical property and corrosion resistance of magnesium alloys [31], by impeding the slip of dislocations and delay of the initiation of corrosion pits. The stress–strain curves of the cast and extruded alloys were shown in Fig. 4. In comparison with cast alloys, the average ultimate tensile strength (UTS) of the extruded Mg–1.21Li–1.12Ca–1Y alloy increases from 51.71 MPa to 183.72 MPa, and yielding strength (YS) from 44.00 MPa to 115.02 MPa and the elongation to failure (EL) of the cast alloy and the extruded alloy is 1.47% and 14.45%, respectively. The significant improvement in the strength and ductility after the extrusion is ascribed to a decrease in grain size and the more dispersive intermetallic compounds, particularly the Mg_2Ca phase.

3.3. Change in corrosion rate

The immersion test shows that the average rates of weight loss of the cast and extruded alloys are 0.24 mg/cm^2/h and 0.18 mg/cm^2/h after an immersion in Hank's solution for 480 min. The corrosion resistance of the extruded alloy was

Table 1
Composition of Hank's solution, g/L.

NaCl	KCl	$CaCl_2$	$NaHCO_3$	Glucose	$MgCl_2•6H_2O$	$MgSO_4•7H_2O$	KH_2PO_4	$Na_2HPO_4•12H_2O$
8.0	0.4	0.14	0.35	1.0	0.1	0.1	0.06	0.126

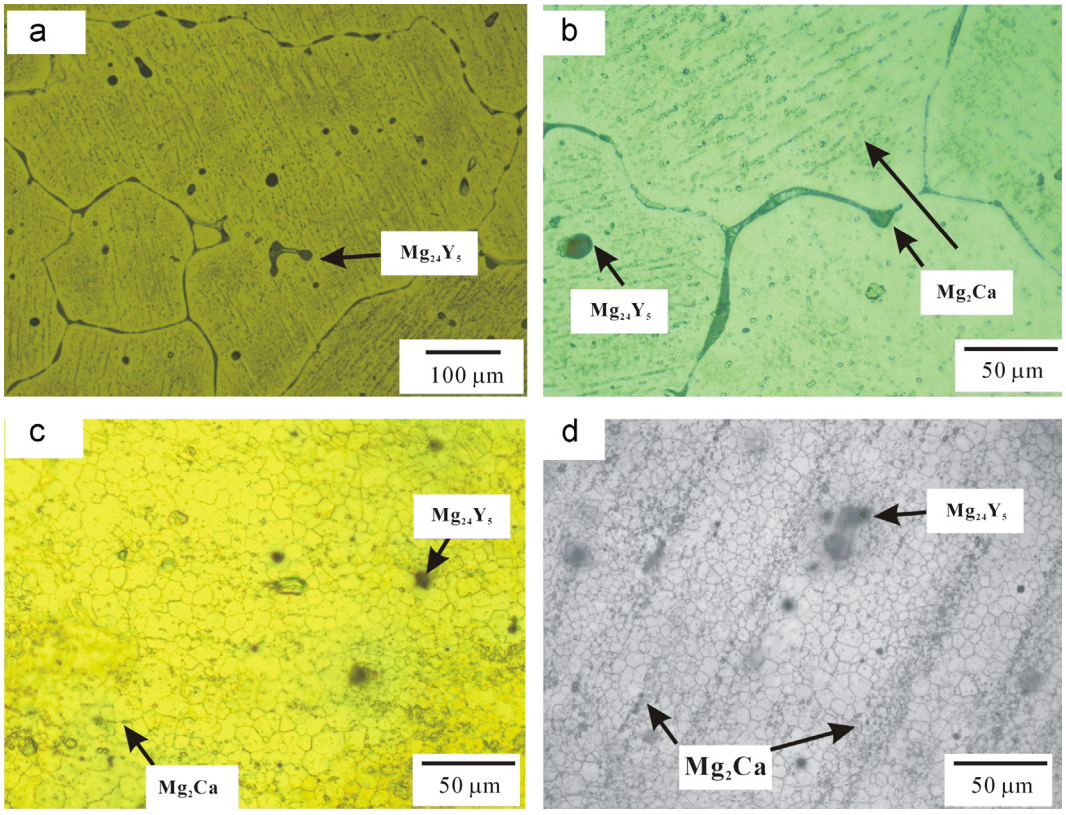

Fig. 1. Optical micrographs: (a) the low and (b) high magnitude of the as-cast Mg–1.21Li–1.12Ca–1Y alloy; (c) the longitudinal view and (d) cross-sectional view of the as-extruded alloys.

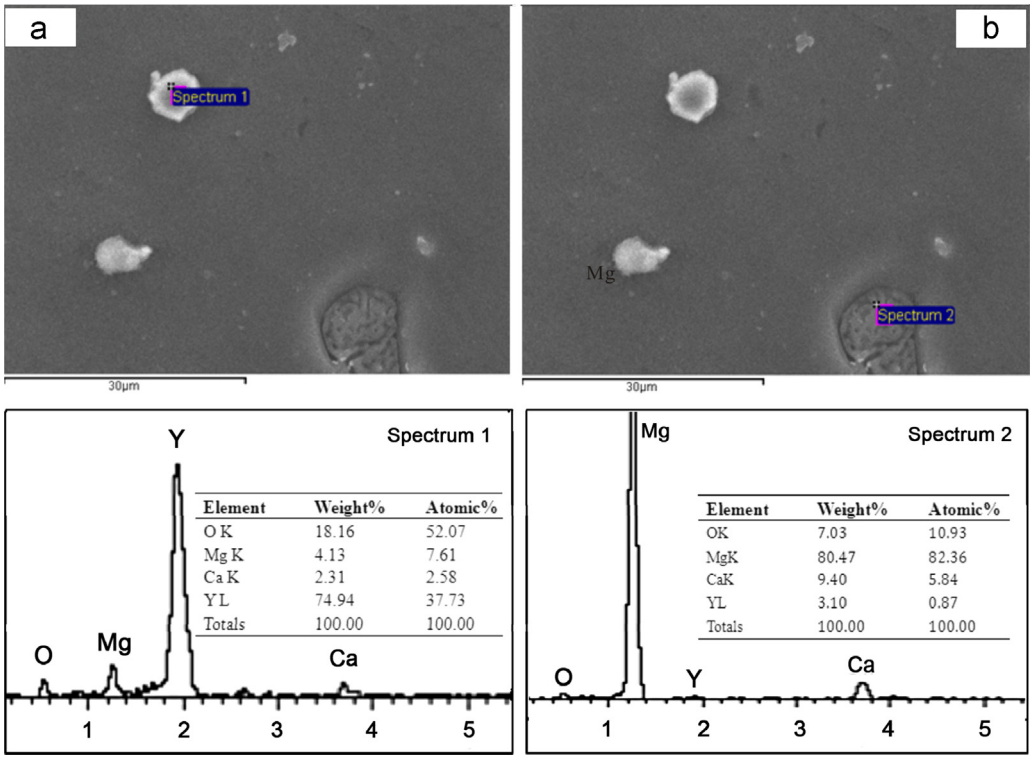

Fig. 2. SEM images and EDS spectrum of the intermetallic compounds of the as-cast alloy: (a), $Mg_{24}Y_5$ particle in the grain interior, and (b) Mg_2Ca particles at GBs.

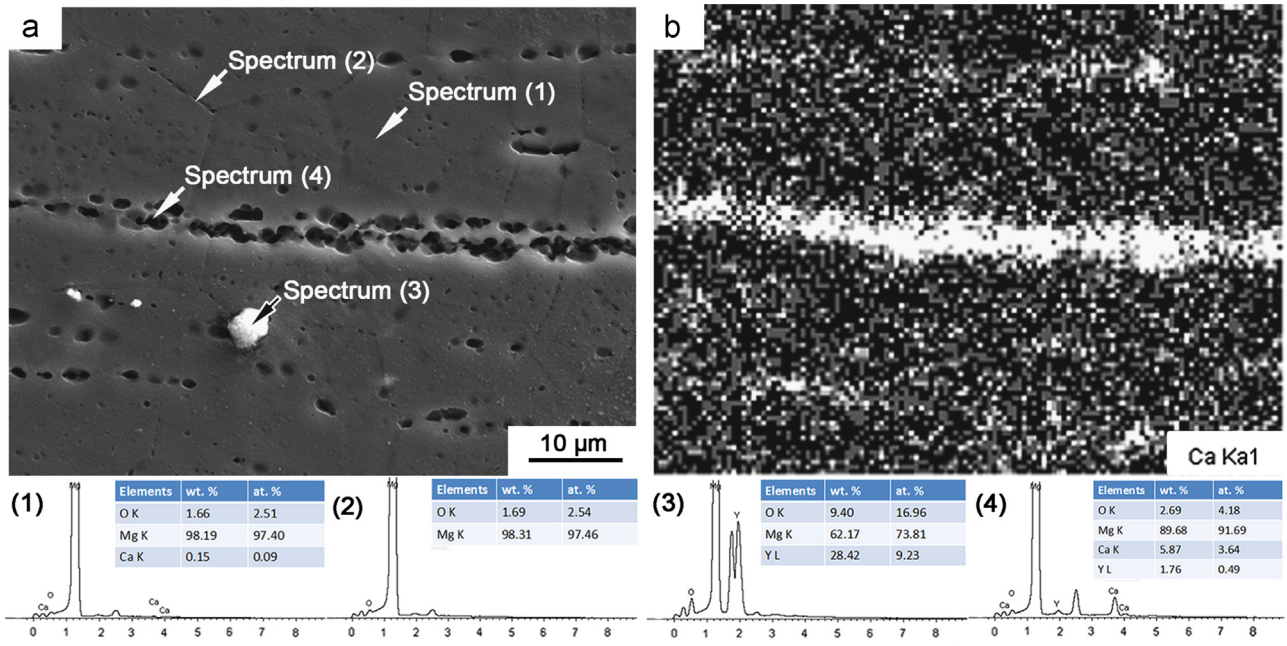

Fig. 3. EPMA images and EDS spectrum of the intermetallic compounds of the as-extruded alloy (a): (1) the grain, (2) the grain boundary, (3) the white granular and (4) the pear-chain-like structure, and (b) area mapping of Ca element.

Table 2
EDS results of the extruded Mg–1.21Li–1.12Ca–1Y alloy in Fig. 3, at%.

Elements	Spectrum 1	Spectrum 2	Spectrum 3	Spectrum 4
O	2.51	2.54	16.96	4.18
Mg	97.40	97.46	73.81	91.69
Ca	0.09	–	–	3.64
Y	–	–	9.23	0.49

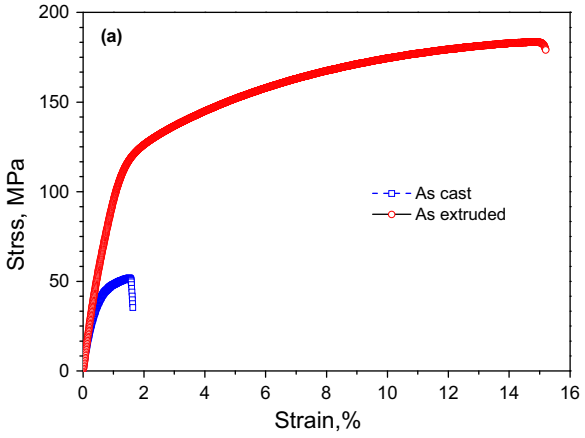

Fig. 4. Tensile stress vs. strain curves of the cast and extruded Mg–1.21Li–1.12Ca–1Y alloys.

evidently lower than that of the cast alloy due to the fine grained microstructure.

Electrochemical measurement results (Fig. 5) also support this result. The free corrosion potentials of the extruded Mg–1.21Li–1.12Ca–1Y alloy and the cast one are −1.67 V vs. SCE and −1.69 V vs. SCE, respectively. The corrosion current densities (6.67×10^{-5} A/cm^2) of the extruded alloy are slightly smaller than that (8.44×10^{-5} A/cm^2) of the cast alloy.

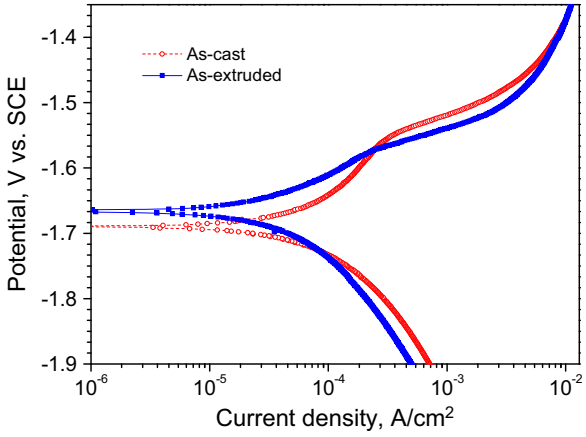

Fig. 5. Polarization curves of the extruded and cast Mg–1.21Li–1.12Ca–1Y alloys.

The HERs and pH values of the cast and extruded Mg–1.21Li–1.12Ca–1Y alloys in Hank's solution have been shown in Fig. 6. Obviously, the change in HER over time in Hank's solution exhibits three stages. In the initial stage of immersion, the HERs of both alloys enhanced rapidly, and then reached up to a fluctuating level. However, the pH values of the solution increase steadily. In the final stage of immersion, the HERs have a tendency to decline continuously.

The immersion tests (Fig. 6) demonstrate that the corrosion product film has a significant influence on the corrosion rate of Mg–1.21Li–1.12Ca–1Y alloy directly. The scenario is analogous

to our previous investigation on Mg–Li–Ca alloys [30,31]. When the bare substrate metal was subject to the attack in Hank's solution at initial stage, HER was promoted to a high level. The corrosion product film, covered the whole surface of bare metal, retarded the HER, and makes the HER remain stable. The HER declined at the subsequent immersion due to an improvement in pH value of the solution and the thickening of the corrosion product layer. Fig. 7 shows the corrosion morphologies of the samples after the immersion in Hank's solution for 8 h, it is clear that the general corrosion occurred.

4. Discussion

It is known that the corrosion resistance of Mg alloys depends on their compositions, microstructure, oxide film and corrosion product film together with composition of the medium [51]. Our previous investigation has demonstrated that the corrosion product film has a critical influence on the corrosion rate of Mg–Li–Ca alloy [31]. The EPMA images and the EDS results reveal that corrosion pit appeared at α-Mg matrix adjacent to the intermetallic compounds Mg_2Ca (Fig. 8a). The result is confirmed by the inset of the EDS spectrum in Fig. 8a due to the possible presence of the compounds of MgO, $Mg(OH)_2$ and Mg_2Ca.

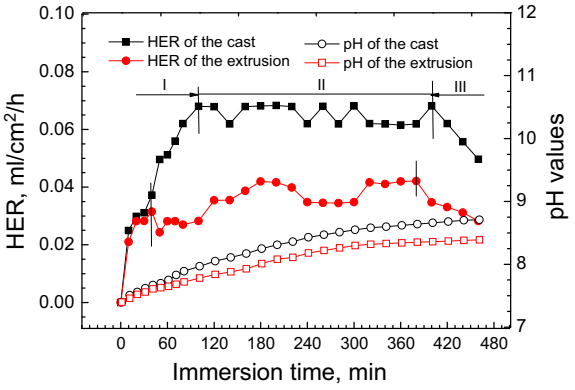

Fig. 6. HERs and pH values of the cast and extruded Mg–1.21Li–1.12Ca–1Y alloys in Hank's solution.

Upon an initial immersion of 15 min, corrosion pits initiated on the substrate, and the HER of Mg–1.21Li–1.12Ca–1Y alloy accelerated (Fig. 6). In subsequent stage of 1 h, corrosion products formed and covered on the corrosion pits and thus prevented the hydrogen release. It is noted that filiform corrosion occurred due to the formation of corrosion product film. Herein the HER of alloy stabilized in a stable level (Fig. 6). In the final immersion stage of 8 h, the HER decreased because of the continuous alkalinization of the solution and the coverage and thickening of the corrosion product layer.

The corrosion product film can be examined on the surfaces of the immersed samples using XRD. The XRD pattern of the Mg–1.21Li–1.12Ca–1Y alloy and the corrosion products formed in Hank's solution for 72 h is shown in Fig. 9. It is clear that the predominant corrosion product is $Mg(OH)_2$ and a little bit of $MgCO_3{\bullet}3H_2O$ existed. Interestingly, the peaks of the corrosion product scale exhibit the formation of noncrystalline or amorphous corrosion products.

Corrosion reactions occur as follows [51]:

Anodic reaction:

$$Mg \rightarrow Mg^{2+} + 2e^{-} \quad (1)$$

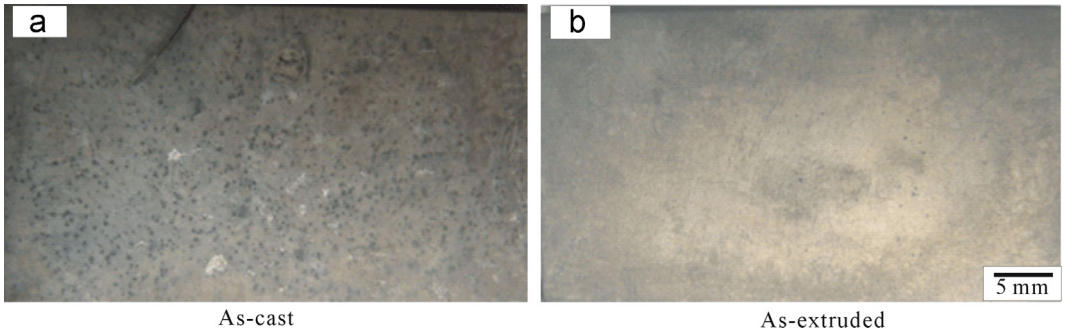

Fig. 7. Corrosion morphologies; (a) and (b) after immersion in Hank's solution for 8 h.

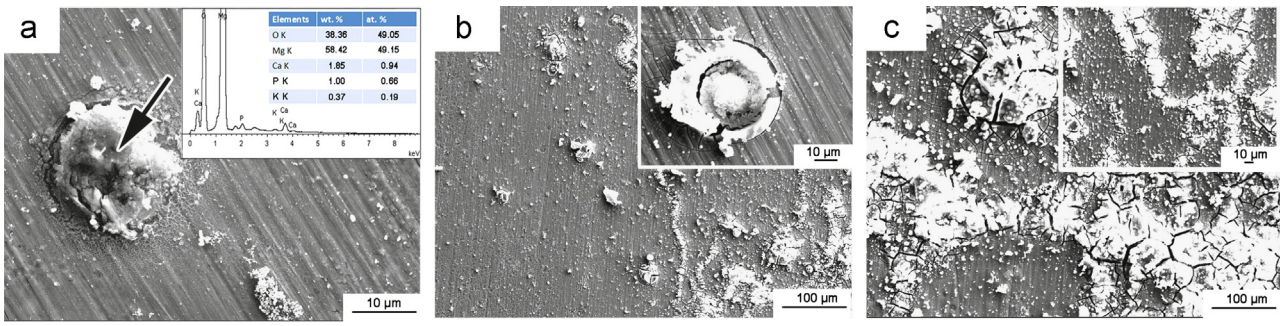

Fig. 8. SEM images of the as-extruded Mg–1.21Li–1.12Ca–1Y alloy after immersion in Hank's solutions for (a) 15 min, (b) 1 h and (c) 8 h.

Cathodic reaction:

$$H_2O + 2e^- \rightarrow 2OH^- + H_2\uparrow \quad (2)$$

Total reaction:

$$Mg + 2H_2O \rightarrow Mg(OH)_2 + H_2\uparrow \quad (3)$$

Hydrolysis reaction of hydrogen carbonates [51]:

$$HCO_3^{2-} + H_2O \leftrightarrow H_2CO_3 + OH^- \quad (4)$$

The formation of the corrosion product layer

$$Mg^{2+} + HCO_3^- + OH^- + (x-1)H_2O \leftrightarrow MgCO_3 \cdot xH_2O (x=3, 5) \quad (5)$$

$$2Mg^{2+} + CO_3^{2-} + 2OH^- \leftrightarrow Mg(OH)_2\downarrow + MgCO_3\downarrow \quad (6)$$

Generally, corrosion rate of Mg alloys relates to their oxide film and corrosion product film. However, the loose precipitate of $Mg(OH)_2$ could provide less protection, which can be solved when it is subject to the attack from Cl^- ions.

$$Mg(OH)_2 + 2Cl^- \leftrightarrow MgCl_2 + 2OH^- \quad (7)$$

Fortunately, the small amount of corrosion products such as $MgCO_3$, $CaCO_3$, Li_2CO_3, $Mg_3(PO_4)_2$, $Ca_3(PO_4)_2$ and Li_3PO_4, resulted in a more dense layer of corrosion products [30,31]. Thus, the corrosion products impede the invasion of the aggressive ions. It should be noted that the PBR of Y_2O_3 is 1.13 and Y element plays a positive role in the enhancement in corrosion resistance of the alloy.

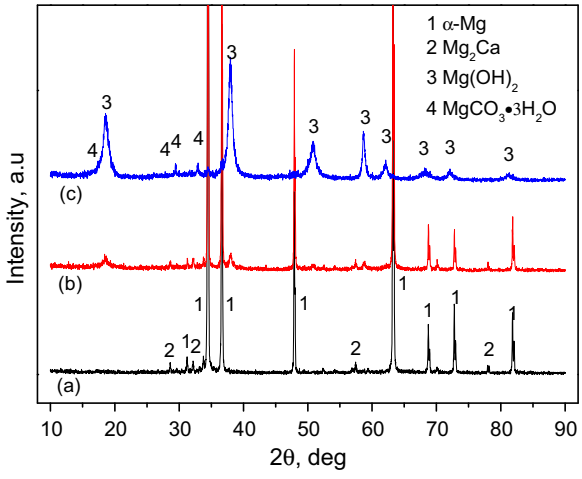

Fig. 9. XRD pattern of (a) the Mg–1.21Li–1.12Ca–1Y substrate, (b) the sample immersed in Hank's solution for 72 h, and (c) the corrosion product scale peeled off from the immersion samples.

Fig. 10 schematically illustrates the mechanism of the corrosion pits generated on the surface of the Mg–1.21Li–1.12Ca–1Y alloy at the initial immersion in Hank's solution. According to the dimension of corrosion pits in SEM image and EDS results (Figs. 8a and 9), corrosion pits initiated at the α-Mg matrix neighboring the Mg_2Ca particles. The corrosion potential for the Mg_2Ca phase was −1.54 V (vs. SCE) and for the α-Mg phase was −2.37 V (vs. NHE) [35]. Thus, a huge potential difference existed between the substrate phase (anode) and intermetallic phase (cathode) led to the micro-galvanic corrosion and accelerated corrosion reaction. Hydrogen generated on the surface of Mg_2Ca particles and Mg^{2+} ion released from α-Mg matrix, as the reaction progressed, $Mg(OH)_2$ precipitation replaced the α-Mg around intermetallic compound and finally encircled Mg_2Ca particle. According to reaction kinetics and dynamics, $Mg(OH)_2$ stably existed when pH > 10.5, interior alkalization of pitting maintained pH value in a pretty high level. There were two sources of $MgCO_3$ precipitation, under alkaline condition, Mg^{2+} ion respectively combined with HCO_3^- and CO_3^{2-} (showed in reactions 5 and 6). HCO_3^- and CO_3^{2-} ions are a common buffer pair in Hank's solution, they can undergo mutual transformation. Therefore, intermetallic Mg_2Ca phase of Mg–1.21Li–1.12Ca–1Y alloy played important role in the corrosion process. However, the influence of intermetallic compound $Mg_{24}Y_5$ particles in the corrosion process still needs further studies.

5. Conclusions

(1) The microstructure of the Mg–1.21Li–1.12Ca–1Y alloy was characterized by α-Mg and intermetallic compound Mg_2Ca and $Mg_{24}Y_5$ particles, most of which distributed along the grain boundaries for the as-cast alloy and the extrusion direction for the as-extruded one.

(2) The tensile mechanical properties including UTS, YS and EL, and the corrosion resistance of the Mg–1.21Li–1.12Ca–1Y alloy were promoted by the extrusion process due to the refined microstructure and the delay of the initiation of corrosion pits.

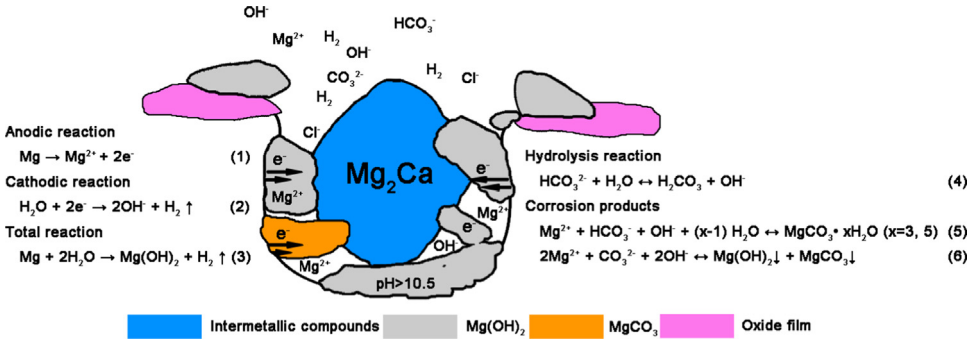

Fig. 10. Schematic diagram of corrosion pits occurred at the intermetallic compound Mg_2Ca on surface of the Mg–1.21Li–1.12Ca–1Y alloy.

(3) Alloying elements (such as Li and Y) play a positive role in corrosion resistance. At the initial stage, the corrosion pits initiated in the α-Mg matrix adjacent to the Mg_2Ca particles. Subsequently, the amorphous corrosion product layer, predominantly composed of $Mg(OH)_2$ and $MgCO_3$, become compact and thick over time, hinder the attack on the magnesium substrate from the aggressive ions, exhibiting a general corrosion and filiform corrosion.

A long-period immersion test will be made to further understand the influence of corrosion product layer on corrosion behavior of the alloy.

Acknowledgments

This research was financially supported by National Natural Science Foundation (NSF) of China (51241001), NSF of Shandong Province (ZR2011EMM004), SDUST Research Fund (2014TDJH104), Joint Innovative Center for Safe and Effective Mining Technology and Equipment of Coal Resources and Taishan Scholarship Project of Shandong Province (TS20110828). Thanks also go to Prof. Rong-Shi Chen at the Institute of Metals Research, Chinese Academy of Sciences for his preparation in the ingots and undergraduate Miss Furong Zhang, graduates Mr. Meng Wang and Mr. Jun Wang at Chongqing University of Technology for their help in the metallurgical, tensile and corrosion tests.

References

[1] Y. Xin, T. Hu, P. Chu, Acta Biomater. 7 (2011) 1452–1459.
[2] M.P. Staiger, A.M. Pietak, J. Huadmai, G. Dias, Biomaterials 27 (2006) 1728–1734.
[3] F. Witte, Acta Biomater. 6 (2010) 1680–1692.
[4] R.C. Zeng, W. Dietzel, F. Witte, N. Hort, C. Blawert, Adv. Eng. Mater. 10 (2008) B3–B14.
[5] R.C. Zeng, L.H. Kong, J. Chen, H.Z. Cui, C.L. Liu, J. Chin. Nonferr. Met. 1 (2011) 35–43.
[6] C.Y. Zang, R.C. Zeng, C.L. Liu, J.C. Gao, Surf. Coat. Technol. 204 (2010) 3636–3640.
[7] C.Y Zang, R.C. Zeng, J. Chen, H. Yang, Z.Q. Tian, Rare Met. Mater. Eng. 8 (2009) 012.
[8] C.Y. Zhang, R.C. Zeng, R.S Chen, C.L. Liu, J.C. Gao, Trans. Nonferr. Met. Soc. China 20 (2010) s655–s659.
[9] R.C. Zeng, Z.D. Lan, L.H. Kong, Y.D. Huang, H.Z. Cui, Surf. Coat. Technol. 205 (2011) 3347–3355.
[10] Y.W. Song, D.Y. Shan, R.S. Chen, F. Zhang, E.H. Han, Surf. Coat. Technol. 203 (2009) 1107–1113.
[11] J.N. Li, P. Cao, X.N. Zhang, S.X. Zhang, Y.H. He, J. Mater. Sci. 45 (2010) 6038–6045.
[12] L.P. Xu, A. Yamamoto, Appl. Surf. Sci. 258 (2012) 6353–6358.
[13] Y.H. Wu, N. Li, Y. Cheng, Y.F. Zheng, Y. Han, J. Mater. Sci. Technol. 29 (2013) 545–550.
[14] J. Chen, R.C. Zeng, W.J. Huang, Z.Q. Zheng, Z.L. Wang, J. Wang, Trans. Nonferr. Met. Soc. China 18 (2008) s361–s364.
[15] T.S.N. Sankara Narayanan, I.S. Park, M.H. Lee, Prog. Mater. Sci. 60 (2014) 1–71.
[16] H. Waizy, J.M. Seitz, J. Reifenrath, A. Weizbauer, F.W. Bach, A. Meyer-Lindenberg, et al., J. Mater. Sci. 48 (2012) 39–50.
[17] Z. Li, X. Gu, S. Lou, Y. Zheng, Biomaterials 29 (2008) 1329–1344.
[18] C.L. Liu, Y.J. Wang, R.C. Zeng, X.M. Zhang, W.J. Huang, P.K. Chu, Corros. Sci. 52 (2010) 3341–3347.
[19] X.N. Gu, Y.F. Zheng, S.P. Zhong, T.F. Xi, J.Q. Wang, W.H. Wang, Biomaterials 31 (2010) 1093–1103.
[20] H.X. Wang, S.K. Guan, X. Wang, C.X. Ren, L.G. Wang, Acta Biomater. 6 (2010) 1743–1748.
[21] L.P. Xu, G.N. Yu, E.L. Zhang, F. Pan, K. Yang, J. Biomed. Mater. Res. A 83 (2007) 703–711.
[22] X.B. Zhang, G.Y. Yuan, L. Mao, J.L. Niu, P.H. Fu, W.J. Ding, J. Mech. Behav. Biomed. 7 (2012) 77–86.
[23] X.B. Zhang, G.Y. Yuan, J.L. Niu, P.H. Fu, W.J. Ding, J. Mech. Behav. Biomed. 9 (2012) 153–162.
[24] E.L. Zhang, L. Yang, Mater. Sci. Eng. A 497 (2008) 111–118.
[25] F. Witte, J. Fischer, J. Nellesen, H.A. Crostack, V. Kaese, A. Pisch, et al., Biomaterials 27 (2006) 1013–1018.
[26] F. Witte, I. Abeln, E. Switzer, V. Kaese, A. Meyer-Lindenberg, H. Windhagen, J. Biomed. Mater. Res. A 86 (2008) 1041–1047.
[27] B. Jiang, X.H. Liu, R.Z. Wu, M.L. Zhang, Z.K. Qu, J.J. Zhu, et al., J. Shanghai Jiaotong Univ. 17 (2012) 297–300.
[28] J.M. Seitz, E. Wulf, P. Freytag, D. Bormann, F.W. Bach, Adv. Eng. Mater. 12 (2010) 1099–1105.
[29] W.R Zhou, Y.F. Zheng, M.A. Leeflang, J. Zhou, Acta Biomater. 9 (2013) 8488–8498.
[30] R.C Zeng, X.L. Guo, C.L. Liu, H.Z. Cui, W. Tao, Y.Y. Liu, B.W. Li, Acta Metall. Sin. 47 (2011) 1477–1482.
[31] R.C. Zeng, L. Sun, Y.F. Zheng, H.Z. Cui, E.H. Han, Corros. Sci. 79 (2014) 69–82.
[32] D. Regenera, V. Tkachenko, Strength Mater. 41 (2009) 294–302.
[33] D.X. Cao, L. Wu, Y. Sun, G. Wang, Y.Z. Lv, J. Power Sources 177 (2008) 624–630.
[34] G.L. Song, Corros. Sci. 49 (2007) 1696–1701.
[35] W.C. Kim, J.G. Kim, J.Y. Lee, H.K. Seok, Mater. Lett. 62 (2008) 4146–4148.
[36] Y. Li, P.D. Hodgson, C.E. Wen, J. Mater. Sci. 46 (2011) 365–371.
[37] Y.F. Ding, C.E. Wen, P. Hodgson, Y.C. Li, J. Mater. Chem. B 2 (2014) 1912–1933.
[38] F. Witte, V. Kaese, H. Haferkamp, E. Switzer, A. Meyer-Lindenberg, C.J. Wirth, et al., Biomaterials 26 (2005) 3557–3563.
[39] H. Ardelean, A. Seyeux, S. Zanna, F. Prima, I. Frateur, P. Marcus, Corros. Sci. 73 (2013) 196–207.
[40] X. Zhang, Y.J. Lij, K. Zhang, C.S. Wang, H.W. Li, M.L. Ma, et al., Trans. Nonferr. Met. Soc. China 23 (2013) 1226–1236.
[41] X. Zhang, K. Zhang, X. Deng, H.W. Li, Y.J Li, M.L. Ma, N. Li, Y.L. Wang, Prog. Nat. Sci.: Mater. Int. 22 (2012) 169–174.
[42] B. Jiang, Y. Zeng, H.M Yin, R.H. Li, F.S. Pan, Prog. Nat. Sci.: Mater. Int. 22 (2012) 160–168.
[43] Q.M. Peng, Y.D. Huang, L. Zhou, N. Hort, K.U. Kainer, Biomaterials 31 (2010) 398–403.
[44] M.X. Zhang, P. Kelly, Scr. Mater. 48 (2003) 379–384.
[45] Y. Xin, T. Hu, P.K. Chu, Acta Biomater. 7 (2011) 1452–1459.
[46] F. Witte, N. Hort, C. Vogt, S. Cohen, K.U. Kainer, R. Willumeit, et al., Curr. Opin. Solid State Mater. Sci. 12 (2008) 63–72.
[47] G.L. Liu, Acta Phys. Sin. 59 (2010) 2708–2713.
[48] W.W. He, E.L. Zhang, K. Yang, Mater. Sci. Eng. C 30 (2010) 167–174.
[49] Y.C. Li, M.H. Li, W.Y. Hu, P.D. Hodgson, C.E. Wen, Mater. Sci. Forum 654 (2010) 2192–2195.
[50] R.C. Zeng, Y. Hu, S.K. Guan, H.Z. Cui, E.H. Han, Corros. Sci. 86 (2014) 171–182.
[51] R.C. Zeng, W.Q. Zhou, E.H. Han, W. Ke, Acta Metall. Sin. 41 (2005) 307–311.